

Ordered Vacancy Induced Cation Intercalation into Layered Double Hydroxides: A General Approach for High-Performance Supercapacitors

Zhenhua Li,^{‡1} Haohong Duan,^{‡2} Mingfei Shao,^{*1} Jianbo Li,¹ Dermot O'Hare,²

Min Wei,^{*1} Zhong Lin Wang^{*3,4}

¹*State Key Laboratory of Chemical Resource Engineering, Beijing University of Chemical Technology, Beijing 100029, China*

²*Chemistry Research Laboratory, Department of Chemistry, University of Oxford, 12 Mansfield Road, Oxford, OX1 3TA, UK*

³*Beijing Institute of Nanoenergy and Nanosystems, Chinese Academy of Sciences, Beijing 100083, China*

⁴*School of Materials Science and Engineering, Georgia Institute of Technology, Atlanta, GA 30332-0245, USA*

[‡]These authors contribute equally to this work.

^{*}Corresponding authors.

E-mail addresses: shaomf@mail.buct.edu.cn (Mingfei Shao); weimin@mail.buct.edu.cn (Min Wei); zlwang@binn.cas.cn (Zhong Lin Wang).

Abstract: New type of cations storage materials would show tremendous potential in the development of high-performance rechargeable energy storage devices. Herein, we develop layered double hydroxides (LDHs) as promising cations supercapacitor materials in aqueous and neutral operation, *via* an effective electrochemical activation strategy, for a reversible intercalation of a wide range of metal cations (*e.g.*, monovalent Li^+ , Na^+ , K^+ and divalent Ca^{2+} , Mg^{2+} , Zn^{2+}). These activated LDHs materials exhibit overwhelming metal-ions storage capacities in aqueous electrolytes, owing to the phase transformation of LDH (repulsive to cations) to hydrogen-vacancy-enriched LDH (LDH-H_V , attractive to cations) induced by the electrochemical activation process. The activated LDH-H_V phase provides a two-dimensional open channel with abundant active sites (H_V) for a reversible intercalation of metal-ions, accounting for the significantly enhanced energy storage performance. This vacancy induced cation intercalation into LDHs builds up a general approach for developing earth-abundant transition-metal resource as a prospective energy storage material toward a large variety of cation supercapacitors.

Introduction

Electrochemical energy storage devices (e.g., batteries and supercapacitors (SCs)) are critical to achieve the important goal of clean sustainable energy for portable electronics, electric vehicles and electricity grid systems¹⁻³. For instance, lithium-ion batteries (LIBs) have helped powered the revolution in various portable and smart devices due to their high energy density and long lifetime⁴⁻⁶. However, the high cost and limited terrestrial reservation of lithium have raised great concerns with a continuous growing demand for LIBs in large-scale applications. Recently, developing new type of metal-ions storage materials (suitable for various cations intercalation) has attracted considerable attention, which provide a large utilization extension of metal-ions in energy storage field⁷⁻¹⁰. Moreover, the use of more abundant, lower cost, and electrochemically comparable cations (such as Na^{+11,12}, Mg^{2+13,14} and Al^{3+15,16}) has also emerged as one of the most promising approaches for the discovery and optimization of high-performance rechargeable batteries and SCs. Despite of large potential, up to date, only a few electrode materials have been successively identified for cations (single- and multi-valent) intercalation, such as metal carbides (MXenes)^{17,18}, metal sulfides (MoS₂)^{19,20} and metal oxides (Bi₂O₃)^{21,22}. Consequently, exploitation of earth-abundant, cost-effective and efficient electrode materials for promising energy storage devices remains a critical challenge.

Layered double hydroxides (LDHs), described by the general formula $[M^{2+}_{1-x}M^{3+}_x(OH)_2]^{x+}(A^{n-})_{x/n} \cdot yH_2O$, are typical two-dimensional materials composed of positively-charged brucite-like host layers and charge compensating interlayer anions²³. Previously, LDHs have been proven as faradaic pseudocapacitive materials for alkaline SCs based on the redox property of host layers, but suffer from a low potential window (<0.5 V) and

poor stability due to the strong oxygen evolution reaction in a high pH media^{24,25}. If LDHs can be efficiently cultivated to serve as host matrix for the intercalation of various earth-abundant cations, a new family of electrochemical energy storage materials can be obtained. However, due to the occupation of interlayer gallery by anions and the charge repulsion between positively-charged LDH laminate and cations, the intercalation of cations from aqueous solution into the domain of LDHs has neither been theoretically predicted nor experimentally demonstrated.

Herein, we report an electrochemical strategy for the activation of two-dimensional LDHs, which demonstrates overwhelming metal-ions storage properties. Surprisingly, the electrochemically-activated LDHs exhibit largely enhanced performance in the intercalation of various metal cations (*e.g.*, monovalent Li^+ , Na^+ , K^+ and divalent Ca^{2+} , Mg^{2+} , Zn^{2+}) with a wide potential window of 0–1.0 V *vs.* SCE and relatively large capacitances in aqueous and neutral electrolytes. For instance, the activated CoFe-LDH nanoarray shows a remarkably improved specific capacitance for Li^+ (552 F g⁻¹), Na^+ (545 F g⁻¹), K^+ (714 F g⁻¹), Ca^{2+} (620 F g⁻¹), Mg^{2+} (780 F g⁻¹) and Zn^{2+} (488 F g⁻¹), which is 48, 23, 35, 29, 60 and 45 times larger than that of unactivated CoFe-LDH, respectively. Furthermore, other kinds of 2D hydroxides (*e.g.*, $\text{Co}(\text{OH})_2$) have also been activated by using this method with satisfactory cations storage properties. In addition, both experimental studies and DFT calculations reveal that the hydrogen vacancy in the activated LDH material (LDH-H_v) plays a key role in the intercalation chemistry and energy storage performances. The intercalation induced capacitance in this work, to the best of our knowledge, keeps the highest level compared with other transition metal hydroxides/oxides materials so far in neutral aqueous media.

Results and discussion

Enhanced cations intercalation performance

As a representative example, CoFe-LDH nanoarrays were first studied as a SC material for the intercalation and storage of metal-ions. The hierarchical CoFe-LDH nanoplatelet arrays were synthesized on the surface of foam nickel substrate *via* a facile electrosynthesis method. As shown in Fig. 1a, a uniform coating of CoFe-LDH nanoplatelets (250–300 nm in lateral length and ~8 nm in thickness) are perpendicularly grafted on the substrate to form an interconnected network with an open and porous structure (Fig. 1b and Supplementary Fig. 1a). EDX mapping analysis (Supplementary Fig. 1b) displays a homogeneous distribution of both cobalt and iron. The XRD pattern shows typical peaks at 2θ 11.59° and 22.68°, which can be indexed to the (003) and (006) reflections of the LDH material (Fig. 1c). Subsequently, an electrochemical activation (ECA) process was carried out by using a facile cyclic voltammetry (CV) method at a scan rate of 100 mV s⁻¹ with different operation potential windows in 1 M KOH solution (Supplementary Fig. 2). It can be seen that the CV curve of CoFe-LDH enlarges gradually with the increase of potential window until a voltage of 0.6 V *vs.* SCE. When the applied potential is larger than 0.6 V, the CV curve shows no expansion and the increased current is due to the electrocatalytic H₂O splitting. For a given ECA potential window, the CV curve reaches a stable level after about 5-cycle tests (Supplementary Fig. 3), implying the complete activation of CoFe-LDH. The cations intercalation properties of the as-obtained ECA-CoFe-LDH electrode within different activation potential ranges were investigated by CV measurement in 2 M LiNO₃ aqueous solution. As shown in Fig. 1d, the CV curve of the ECA-

CoFe-LDH in neutral LiNO₃ electrolyte enlarges gradually along with the increase of activation potential and reaches a maximum with a potential window of 0–0.6 V *vs.* SCE (denoted as ECA(0.6V)-CoFe-LDH), indicating a largely enhanced capacitance. In contrast, the initial CoFe-LDH without ECA treatment is almost electrochemically inactive in the LiNO₃ solution. It should be noted that there is no assistance to improve the supercapacitive properties of CoFe-LDH by just immersing this material in 1 M KOH solution for 24 h (Supplementary Fig. 4).

Fig. 1e shows the galvanostatic (GV) charge/discharge curves of ECA-CoFe-LDH electrode at a current density of 2 A g⁻¹ in LiNO₃ electrolyte. The ECA(0.6V)-CoFe-LDH exhibits a specific capacitance of 552 F g⁻¹ (55.2 F cm⁻³) at 2 A g⁻¹, which is 48 times larger than that of initial CoFe-LDH electrode (11.5 F g⁻¹). Rate capability is a key parameter for the evaluation of supercapacitors, which was determined by using the GV technique at different charge/discharge current densities. Within the whole current density range (Supplementary Fig. 5), the ECA(0.6V)-CoFe-LDH yields substantially higher specific capacitance than samples pretreated with a small ECA potentials (Supplementary Table 1). At a high current density of 40 A g⁻¹, the specific capacitance of ECA(0.6V)-CoFe-LDH maintains 45%, whilst only 23% is found for the initial CoFe-LDH (Fig. 1f). To elucidate the occurrence of either cations or anions insertion, we used two different lithium salt solution (1 M Li₂SO₄ and 2 M LiNO₃) as electrolytes, and the corresponding CV curves are shown in Supplementary Fig. 6. Clearly, the CV responses in these two solutions (containing different anions) are rather identical, confirming the intercalation of cations other than anions. Furthermore, the ECA(0.6V)-CoFe-LDH electrode shows a linearly enhanced redox current in CV curve upon increasing Li⁺ concentration, indicating the intercalation of Li⁺ (Supplementary Fig. 7). In addition, we studied

the cyclability of the ECA(0.6V)-CoFe-LDH by performing more than 10,000 cycles by GV at a current density of 24 A g^{-1} in LiNO_3 electrolyte. As shown in Fig. 1g, a capacitive retention of 99 % is obtained, and the electrode surface remains its original hierarchical architecture after 10,000 charge/discharge cycles (Supplementary Fig. 8), indicating a satisfactory stability.

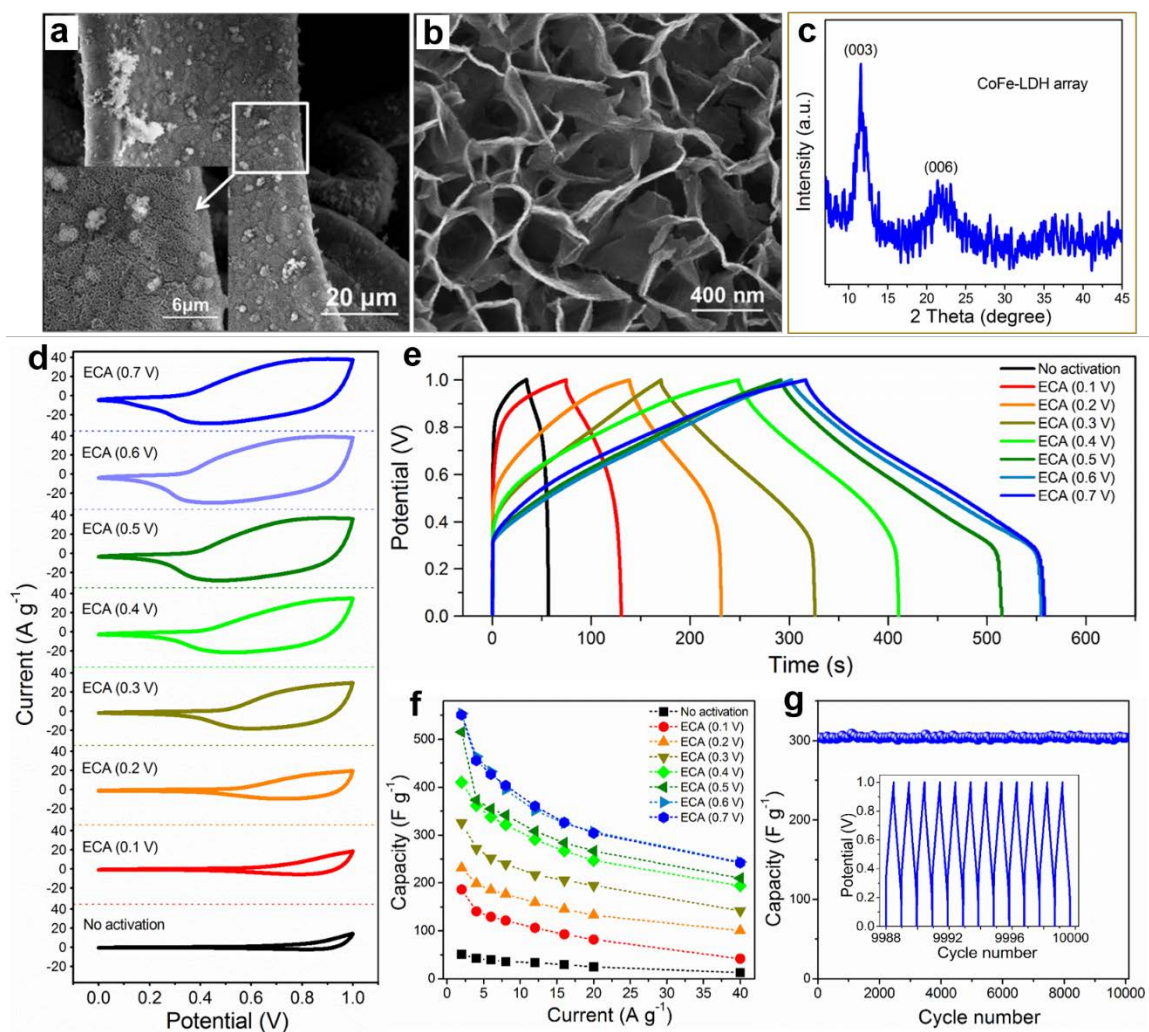


Figure 1 | Enhanced Li^+ intercalation properties of the ECA-CoFe-LDH materials. SEM images of CoFe-LDH nanoplatelet arrays grafted on the foam nickel substrate with (a) low and (b) high magnification, respectively. (c) XRD pattern of the CoFe-LDH array. (d) CV curves of ECA-CoFe-LDH at a scan rate of 50 mV s^{-1} in 2 M LiNO_3 solution. (e) GV charge/discharge measurements of ECA-CoFe-LDH at a current density of 2 A g^{-1} in 2 M LiNO_3 solution. (f) Rate capability of ECA-CoFe-LDH with different ECA process. (g) Capacitive retention of ECA(0.6V)-CoFe-LDH in 2 M LiNO_3 electrolyte after 10,000 cycles at a current density of 24

A g⁻¹.

To study the multi-metal-ions storage property of ECA-CoFe-LDH, CV measurements in different metal salt solutions (*e.g.*, NaNO₃, KNO₃, Ca(NO₃)₂, Mg(NO₃)₂ and Zn(NO₃)₂) were performed. As shown in Fig. 2a, the initial CoFe-LDH is almost electrochemically inactive in the above aqueous solutions. In contrast, the ECA(0.6V)-CoFe-LDH shows a significantly improved intercalation property for these cations. Based on the GV charge/discharge curves at a current density of 2 A g⁻¹, the specific capacitances of ECA(0.6V)-CoFe-LDH for Na⁺, K⁺, Ca²⁺, Mg²⁺ and Zn²⁺ give 545 F g⁻¹, 714 F g⁻¹, 620 F g⁻¹, 780 F g⁻¹ and 488 F g⁻¹, respectively, which are 23, 35, 29, 60 and 45 times larger than the initial CoFe-LDH electrode (Fig. 2b). Moreover, cations intercalation-induced capacitances in this work, are significantly larger than those of previously reported transition metal hydroxides/oxides materials in benign and neutral aqueous electrolyte (Supplementary Fig. 9). The corresponding rate capabilities of ECA(0.6V)-CoFe-LDH determined by GV technique at different charge/discharge current densities also show a satisfactory and comparable intercalation results for these cations (Supplementary Fig. 10). Furthermore, this ECA method is also successfully demonstrated in other two-dimensional Co-based hydroxides, such as: CoNi-LDH, CoAl-LDH and β-Co(OH)₂ nanoplatelets (Fig. 2c, Supplementary Fig. 11), which proves the universality of this method. It is also found that the hydroxide nanoarrays anchoring to conducting substrate exhibit superior energy storage capacity in comparison with corresponding hydroxide nanoparticle samples (Supplementary Fig. 12), which is mostly attributed to the sufficient exposure of active sites and enhanced mass transportation in this hierarchical architecture. In order to confirm the active site in ECA-CoFe-LDH material, we tested the supercapacitive performance of LiFe-LDH electrode in LiNO₃

electrolyte, which showed no any electrochemical activation in metallic salt solutions before and after ECA treatment (Supplementary Fig. 13). This indicates that the Co species play a more important role in the ECA-CoFe-LDH material. It has been reported that the Fe-containing LDHs possess better conductivity than other types of LDHs^{26,27}; therefore, we believe the existence of Fe species would be beneficial to the electron transfer and facilitate the metal-ions migration.

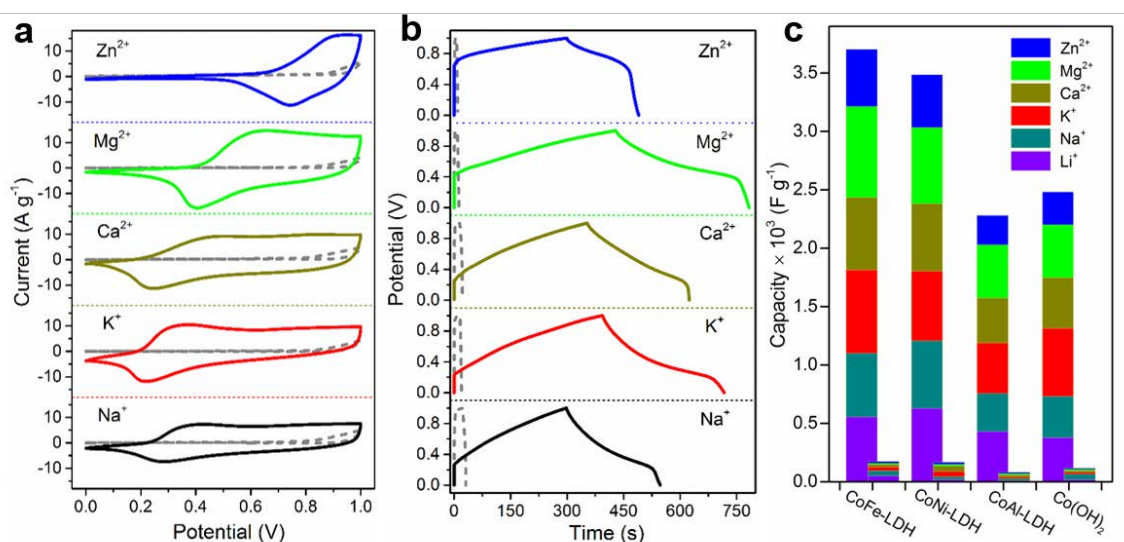


Figure 2 | Multi-metal-ion storage property of 2D Co-based hydroxides. (a) CV curves of ECA(0.6V)-CoFe-LDH and initial CoFe-LDH in different metal salt solutions at a scan rate of 10 mV s⁻¹. (b) Corresponding GV curves of ECA(0.6V)-CoFe-LDH and initial CoFe-LDH in different metal salt solutions at a current density of 2 A g⁻¹. (c) Ions storage property for CoFe-LDH, CoNi-LDH, CoAl-LDH and Co(OH)₂ electrode before and after ECA treatment, respectively.

Discussion

To elucidate the intercalation mechanism, we first studied the changes in structure and composition of CoFe-LDH during the ECA process. The color of CoFe-LDH turns from yellow to dark brown gradually with the increased ECA treatment potential (Supplementary Fig. 14),

implying the oxidation of Co atom in CoFe-LDH. The XRD patterns display a shift of (003) reflection to large angle (Fig. 3a, Supplementary Fig. 15 for full XRD pattern and Supplementary Table 2), indicating a gradual shrinkage in the interlayer distance of ECA-CoFe-LDH along with increased ECA treatment potential. The FTIR spectra show that both the stretching of hydroxide group and interlayer carbonate species decrease gradually (Fig. 3b), illustrating the reduce of hydroxyl group in the CoFe-LDH host layers and the loss of interlayer carbonate. Moreover, the typical broad stretching band of Co–OH (798 cm^{-1}) vanishes gradually, accompanied with the appearance of O–Co–O vibration at 568 cm^{-1} . This demonstrates the conversion of Co in CoFe-LDH from $\text{Co}(\text{OH})_2$ to CoOOH . Furthermore, X-ray photoelectron spectroscopy (XPS) was also employed to examine the changes of the surface chemical states. As shown in Fig. 3c, the initial CoFe-LDH displays a Co $2p_{3/2}$ peak located at 782.38 eV, indicating the existence of Co^{2+} (ref. 29). A new peak at 780.08 eV attributed to Co^{3+} arises after the ECA process^{29,30}, whose intensity enhances gradually with the increasement of ECA potential. The content of Co^{3+} increases from 0.4 % to 92.1 % *via* XPS spectra (Supplementary Table 3), demonstrating the conversion from Co^{2+} to Co^{3+} . The same result is also obtained in the Co $2p_{1/2}$ XPS spectra (Supplementary Fig. 16). Fig. 3d shows the binding energy of O 1s. The initial CoFe-LDH exhibits an OH^- peak at 531.3 eV³¹; after the ECA process, a new peak at 529.5 eV assigned to O^{2-} is observed with increasing intensity^{31,32}, indicating a transition process of O species from OH^- to O^{2-} . Based on the results above, it is concluded that the ECA process leads to the transformation of Co in CoFe-LDH from $\text{Co}(\text{OH})_2$ to CoOOH . As for the Fe element, the binding energies of Fe $2p_{3/2}$ (711.0 eV) and Fe $2p_{1/2}$ (724.9 eV) are observed for the initial CoFe-LDH (Supplementary Fig. 17), corresponding to

the Fe(III) oxidation state³³. After the ECA process, a slight shift to lower energy level (~ 0.5 eV for ECA (0.6V)-CoFe-LDH) is observed, suggesting an electron-accepter property due to the changes of surface electronic environment³⁴. The Co/Fe ratios of the CoFe-LDH and ECA-CoFe-LDH are 1.96, which was studied by inductively coupled plasma-atomic emission spectroscopy (ICP-AES).

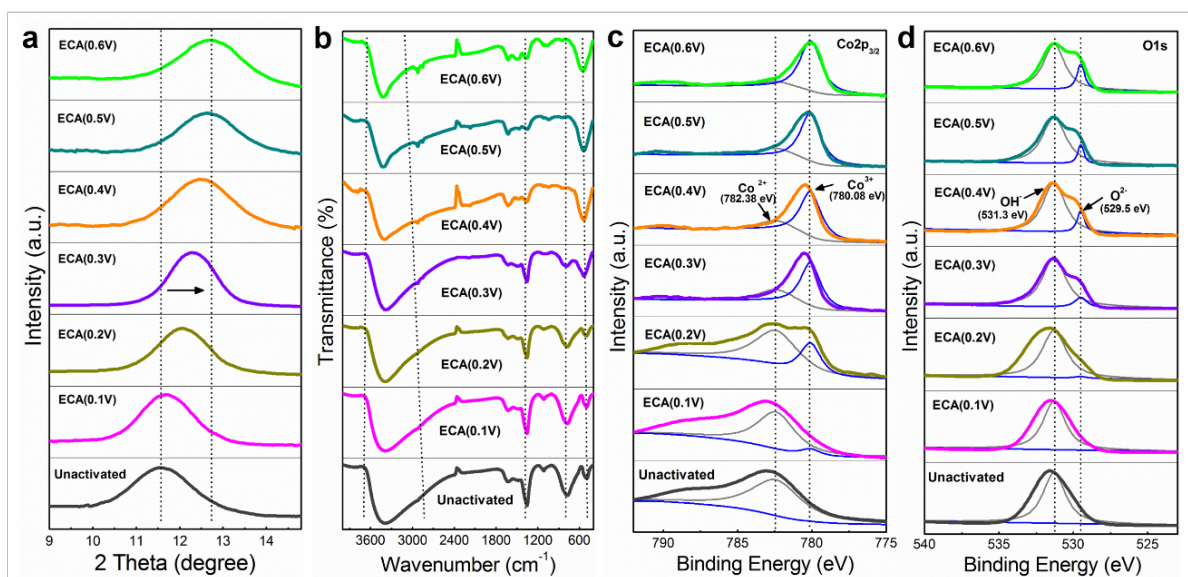


Figure 3 | Structure and composition changes of CoFe-LDH after different ECA process.

(a) XRD patterns of the (003) reflection of CoFe-LDH with different ECA process. (b-d) FTIR spectra (b), high-resolution Co 2p_{3/2} XPS spectra (c) and O 1s spectra (d) of ECA-CoFe-LDH with different ECA process.

X-ray absorption spectroscopy (XAS) was performed to investigate the structural change of ECA-CoFe-LDH. Fig. 4a displays the X-ray absorption near edge structure (XANES) results of ECA-CoFe-LDH with various treatment potential. The white line of initial CoFe-LDH almost coincides with the Co(OH)₂ reference (Supplementary Fig. 18a), indicating that the Co element in CoFe-LDH is predominant as Co(OH)₂ phase. As the ECA potential increases from 0 V to 0.6 V, a shift of the white line toward higher binding energy occurs and a significant

energy shift of 6.3 eV is obtained between ECA(0.6V)-CoFe-LDH and unactivated CoFe-LDH (Supplementary Fig. 19), corresponding to the oxidation of hydroxide $\text{Co}^{2+}\text{-OH}$ to hydroxyloxyde $\text{Co}^{3+}\text{-OOH}$ ³⁵⁻³⁷. Furthermore, the Fourier transform of Co K-edge EXAFS oscillations was further used to study the detailed atomic configuration of ECA(0.6V)-CoFe-LDH (Fig. 4b). In the R-space spectrum of initial CoFe-LDH, the peak centered at 2.10 Å and 3.10 Å are attributed to the Co–O and Co–Co bond distance of Co(OH)_2 (Supplementary Fig. 18b: Co(OH)_2 reference). In contrast, the peak positions of Co–O and Co–Co in ECA(0.6V)-CoFe-LDH shift to 1.90 Å and 2.85 Å, respectively, indicating the formation of Co^{3+} oxyhydroxide³⁵⁻³⁷. Based on the XRD, FTIR, XPS, ICP and XAS results, the activation process of CoFe-LDH and the corresponding structures can be illustrated in Fig. 4c. During the ECA process, $\text{Co}^{2+}(\text{OH})_2$ in CoFe-LDH is gradually oxidized to $\text{Co}^{3+}\text{-OOH}$, which results in a large amount of hydrogen vacancies in the host layers of CoFe-LDH and the removal of carbonate ions from the interlayer region. The corresponding structure formula changes from $[\text{Co}^{2+}_{1-x}\text{Fe}^{3+}_x(\text{OH})_2]^{x+}(\text{CO}_3^{2-})_{x/2} \cdot m\text{H}_2\text{O}$ ($x \approx 1/3$) for the initial CoFe-LDH to $[\text{Co}^{3+}_{1-x}\text{Fe}^{3+}_x\text{O(OH)}] \cdot n\text{H}_2\text{O}$ for the ECA-CoFe-LDH.

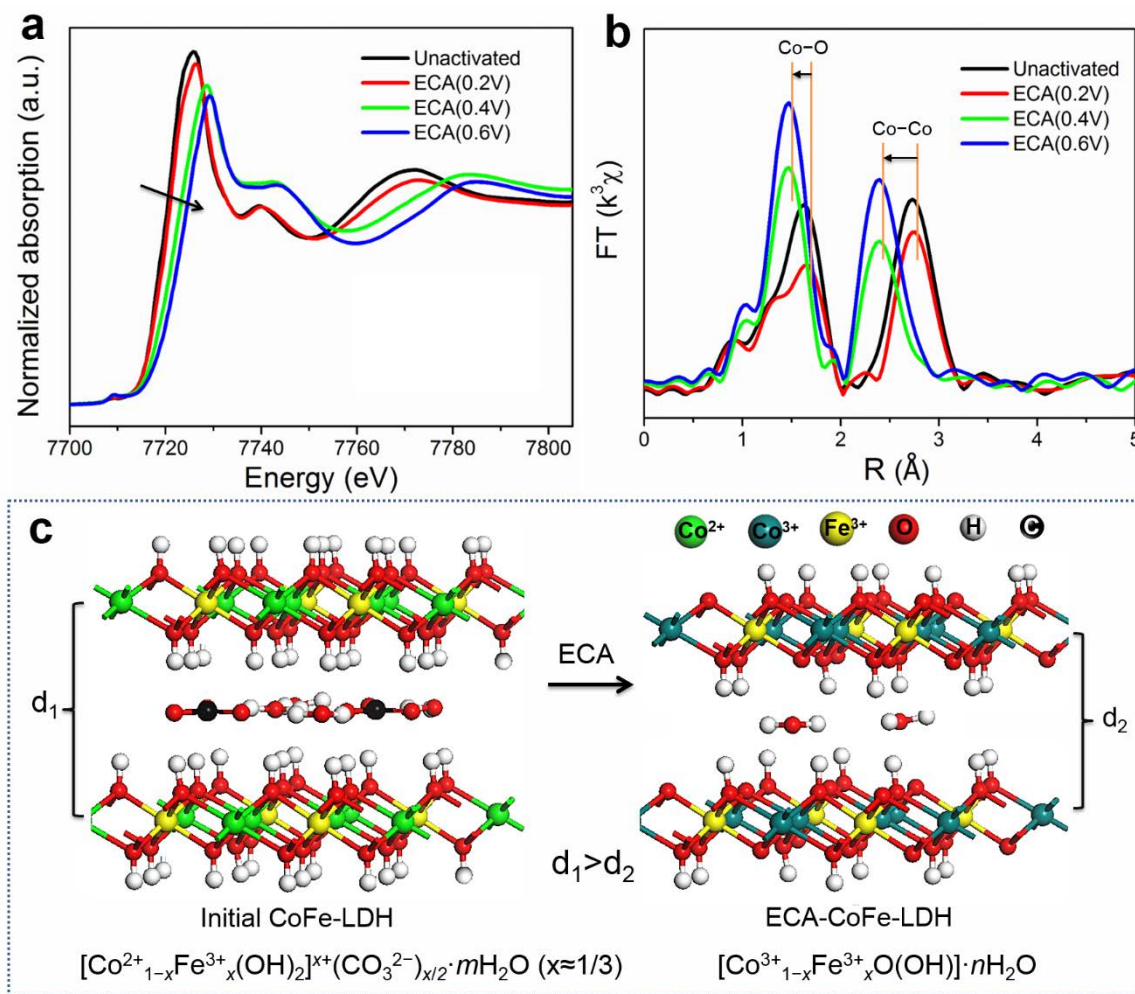


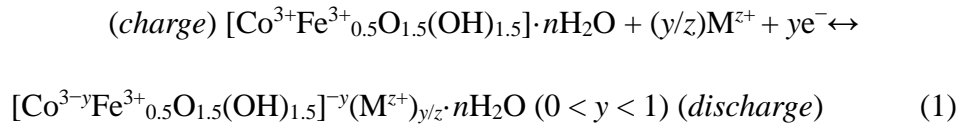
Figure 4 | Structure change investigation and illustration. (a,b) Co K-edge X-ray absorption near-edge structure (XANES) spectra (a) and the corresponding k^2 -weighted Fourier transforms of Co K-edge EXAFS spectra (b) for CoFe-LDH with different ECA potentials. (c) Schematic illustration for the structure and composition change of CoFe-LDH during the ECA process.

The metal ion storage mechanism for ECA-CoFe-LDH was further studied. XRD was used to study the change of interlayer distance during the discharge-charge cycle. It's interesting that the fresh ECA(0.6V)-CoFe-LDH gives a d_{003} of 0.69 nm; while it enlarges to 0.73 nm after the discharge process in LiNO_3 solution and then shrinks to 0.69 nm after a further charge process (Fig. 5a). This demonstrates that the intercalation/extraction of Li^+ leads

to a reversible expansion/shrinkage of the interlayer distance. A similar phenomenon is also observed in other cations discharge-charge cycle (Na^+ , K^+ , Ca^{2+} , Mg^{2+} , Zn^{2+} ; Supplementary Fig. 20). In addition, XPS spectra of ECA(0.6V)-CoFe-LDH show signals of Li^+ , Na^+ , K^+ , Ca^{2+} , Mg^{2+} , Zn^{2+} , respectively, after a discharging process toward these cations (Supplementary Fig. 21), and the peak intensity decreases significantly after the subsequent charging process (Supplementary Fig. 22), further indicating the insertion/removal of metal-ions in ECA(0.6V)-CoFe-LDH during the electrochemical discharge-charge cycling. Further studies over ECA(0.6V)-CoFe-LDH reveal that Co 2p XPS peaks display a reversible shift to a higher energy level (discharging) and recover to its original energy level (charging). This demonstrates that the intercalation of cation causes the decrease of cobalt valence state in ECA-CoFe-LDH and it can be recovered to original valence state (Co^{3+}) after the cation extraction (Fig 5b). Correspondingly, as for the O 1s XPS spectra of the discharged ECA(0.6V)-CoFe-LDH, a new peak at higher binding energy (532.9 eV) is observed with the disappearance of O^{2-} peak at 529.5 eV (Fig. 5c) because of the interaction between oxygen species and the inserted metal-ions, implying the exposed oxygen on the activated LDH layers is the active site for the cations storage.

Density functional theory (DFT) calculations were carried out to further elucidate the adsorption site and adsorption energy of metal-ions (Li^+ , Na^+ , K^+ , Ca^{2+} , Mg^{2+} , Zn^{2+}) in ECA-CoFe-LDH (see computational details in the Supplementary Information). The models are built based on the cations adsorb over LDH host layer with terminal hydrogen or oxygen. The calculated adsorption energies are summarized in Fig. 5d and Supplementary Table 4. It is found that most of the adsorption energies are positive for cations adsorb over the terminal-H,

suggesting that the hydroxide group is unfavorable for the adsorption of metal-ions. In contrast, the LDH layer with O-termination gives negative adsorption energies toward Li^+ , Na^+ , K^+ , Ca^{2+} , Mg^{2+} , Zn^{2+} , which indicates a thermodynamically favorable process. According to the results above, the charging-discharging electrochemical reaction in ECA-CoFe-LDH electrode can be described as follows:



where y/z denotes the number of reversibly intercalated cations (M^{z+}). As shown in Fig. 5e, cations (M^{z+}) insert into the gallery of ECA-CoFe-LDH during discharge process accompanied with the expansion of interlayer distance and the decrease of cobalt valence state. During the charging process, a reversible shrinkage of interlayer distance and recovery of Co valence state can be achieved along with the cations extraction. The H-vacancies adjacent to oxygen in the host matrix of ECA-CoFe-LDH serve as active site for cations embedding.

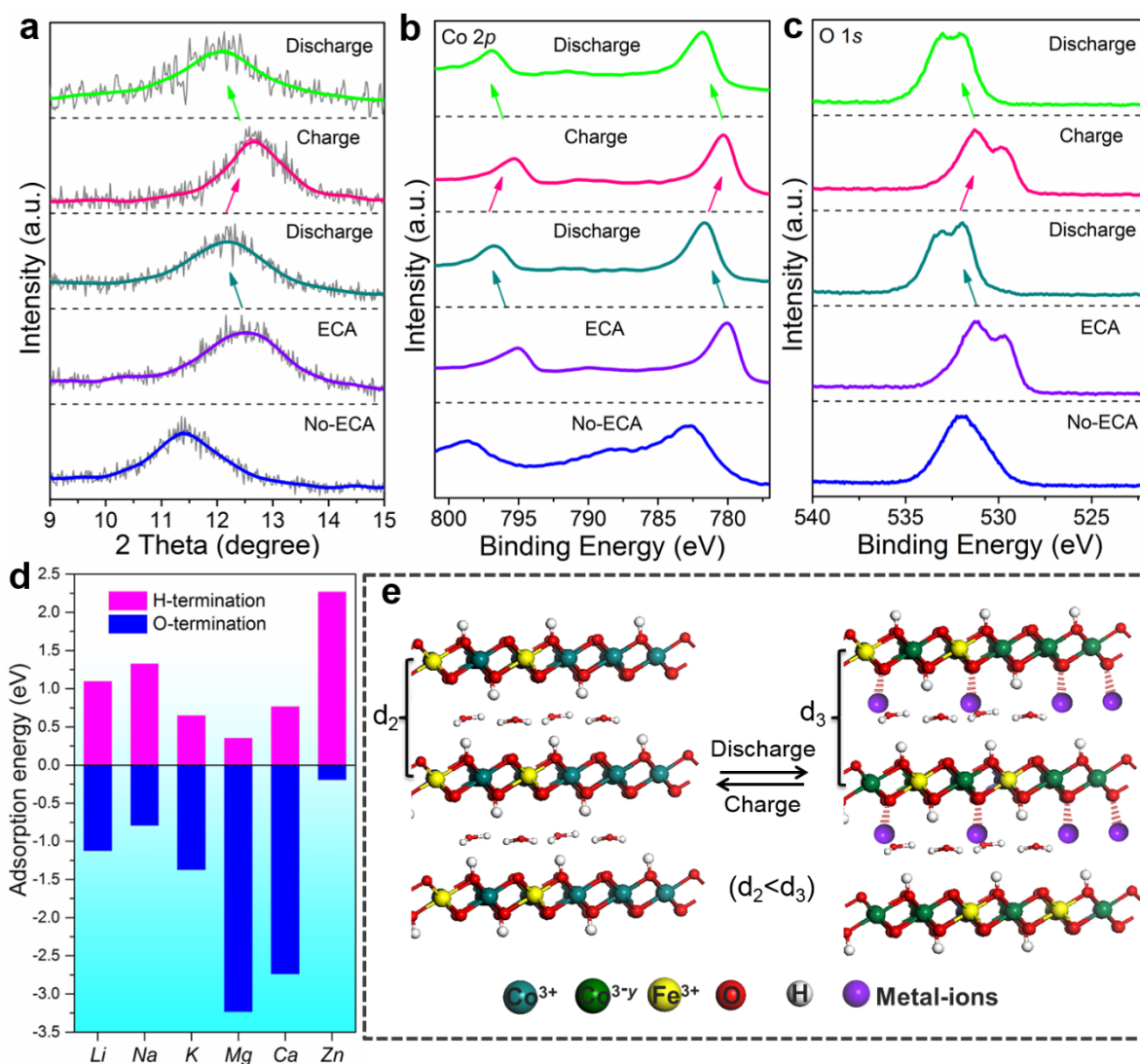


Figure 5 | Study on metal-ions storage mechanism for ECA-CoFe-LDH. (a) XRD patterns for (003) reflection of ECA(0.6V)-CoFe-LDH during Li^+ discharge-charge process. (b,c) High-resolution Co 1p spectra (b) and O 1s spectra (c) of ECA(0.6V)-CoFe-LDH during Li^+ discharge-charge process. (d) Adsorption energies of metal ion over OH-terminated and O-terminated LDH laminate. (e) Schematic illustration for the intercalation/extraction of metal-ions during the discharge/charge cycle over ECA-CoFe-LDH.

Conclusions

In summary, an electrochemical activation strategy has been developed to largely improve the cation storage performances of two-dimensional LDHs materials. The results show that the

ECA process induces the formation of H-vacancies on LDH host layers and extravasation of interlayer anions, which effectively eliminates the electrostatic repulsion between LDHs and cations. Consequently, the activated CoFe-LDH exhibits a reversible cations intercalation/extraction property with remarkably high capacity and cycling stability; the capacities dependent on cations intercalation in this work keep the highest level among previously reported transition metal hydroxides/oxides materials in neutral aqueous electrolyte. This work opens a new avenue for the exploration of universal, promising and cost-effective electrochemical energy storage materials based on 2D transition-metal hydroxides.

Reference

1. Noorden, R. V. A better battery. *Nature* **507**, 26–28 (2014).
2. Dunn, B., Kamath, H. & Tarascon, J.-M. Electrical energy storage for the grid: a battery of choices. *Science* **334**, 928–935 (2011).
3. Simon, P., Gogotsi, Y. & Dunn, B. Where do batteries end and supercapacitors begin? *Science* **343**, 1210–1211 (2014).
4. Wang, C. *et al.* Self-healing chemistry enables the stable operation of silicon microparticle anodes for high-energy lithium-ion batteries. *Nat. Chem.* **5**, 1042–1048 (2013).
5. Goodenough, J. B. & Park, K.-S. The Li-ion rechargeable battery: a perspective. *J. Am. Chem. Soc.* **135**, 1167–1176 (2013).
6. Etacheri, V., Marom, R., Elazari, R., Salitra, G. & Aurbach, D. Challenges in the development of advanced Li-ion batteries: a review. *Energy Environ. Sci.* **4**, 3243–3262 (2011).

7. Islam, M. S. & Fisher, C. A. J. Lithium and sodium battery cathode materials: computational insights into voltage, diffusion and nanostructural properties. *Chem. Soc. Rev.* **43**, 185–204 (2014).
8. Zhang, H. Ultrathin two-dimensional nanomaterials. *ACS Nano* **9**, 9451–9469 (2015).
9. Brezesinski, T., Wang, J., Tolbert, S. H. & Dunn, B. Ordered mesoporous α -MoO₃ with iso-oriented nanocrystalline walls for thin-film pseudocapacitors. *Nat. Mater.* **9**, 146–151 (2010).
10. Zhang, Q., Huang, J., Qian, W., Zhang, Y. & Wei, F. The road for nanomaterials industry: a review of carbon nanotube production, post-treatment, and bulk applications for composites and energy storage. *Small* **9**, 1237–1265 (2013).
11. Sun, J. *et al.* A phosphorene–graphene hybrid material as a high-capacity anode for sodium-ion batteries. *Nat. Nanotechnol.* **10**, 980–985 (2015).
12. Yabuuchi, N., Kubota, K., Dahbi, M. & Komaba, S. Research development on sodium-ion batteries. *Chem. Rev.* **114**, 11636–11682 (2014).
13. Shao, Y. *et al.* Highly reversible Mg insertion in nanostructured Bi for Mg ion batteries. *Nano Lett.* **14**, 255–260 (2014).
14. Yoo, H. D. *et al.* Mg rechargeable batteries: An on-going challenge. *Energy Environ. Sci.* **6**, 2265–2279 (2013).
15. Lin, M.-C. *et al.* An ultrafast rechargeable aluminium-ion battery. *Nature* **520**, 324–328 (2015).
16. Yu, X., Wang, B., Gong, D., Xu, Z. & Lu, B. Graphene nanoribbons on highly porous 3D graphene for high-capacity and ultrastable Al-ion batteries. *Adv. Mater.* **29**, 1604118 (2017).

17. Lukatskaya, M. R. *et al.* Cation intercalation and high volumetric capacitance of two-dimensional titanium carbide. *Science* **341**, 1502–1505 (2013).
18. Wang, X. *et al.* Pseudocapacitance of MXene nanosheets for high-power sodium-ion hybrid capacitors. *Nat. Commun.* **6**, 6544 (2015).
19. Acerce, M., Voiry, D. & Chhowalla, M. Metallic 1T phase MoS₂ nanosheets as supercapacitor electrode materials. *Nat. Nanotechnol.* **10**, 313–318 (2015).
20. Wang, X., Shen, X., Wang, Z., Yu, R. & Chen, L. Atomic-scale clarification of structural transition of MoS₂ upon sodium intercalation. *ACS Nano* **8**, 11394–11400 (2014).
21. Zuo, W. *et al.* Bismuth oxide: a versatile high-capacity electrode material for rechargeable aqueous metal-ion batteries. *Energy Environ. Sci.* **9**, 2881–2891 (2016).
22. Li, Y. *et al.* Bismuth oxide: a new lithium-ion battery anode. *J. Mater. Chem. A* **1**, 12123–12127 (2013).
23. Shao, M. *et al.* Layered double hydroxides toward electrochemical energy storage and conversion: design, synthesis and applications. *Chem. Commun.* **51**, 15880–15893 (2015).
24. Li, Z. *et al.* A flexible all-solid-state micro-supercapacitor based on hierarchical CuO@layered double hydroxide core–shell nanoarrays. *Nano Energy* **20**, 294–304 (2016).
25. Liu, X., Ma, R., Bando, Y. & Sasaki, T. A general strategy to layered transition-metal hydroxide nanocones: tuning the composition for high electrochemical performance. *Adv. Mater.* **24**, 2148–2153 (2012).
26. Song, F. & Hu, X. Exfoliation of layered double hydroxides for enhanced oxygen evolution catalysis. *Nat. Commun.* **5**, 4477 (2014).
27. Trotochaud, L., Young, S. L., Ranney, J. K. & Boettcher, S. W. Nickel–iron oxyhydroxide

- oxygen-evolution electrocatalysts: the role of intentional and incidental iron incorporation. *J. Am. Chem. Soc.* **136**, 6744–6753 (2014).
28. Lukowski, M. A. *et al.* Enhanced hydrogen evolution catalysis from chemically exfoliated metallic MoS₂ nanosheets. *J. Am. Chem. Soc.* **135**, 10274–10277 (2013).
 29. Yang, J., Liu, H., Martens, W. N. & Frost, R. L. Synthesis and characterization of cobalt hydroxide, cobalt oxyhydroxide, and cobalt oxide nanodiscs. *J. Phys. Chem. C* **114**, 111–119 (2009).
 30. Hu, M., Ji, X., Lei, L. & Lu, X. Structural and electrochemical stability of CoAl layered double hydroxide in alkali solutions. *Electrochim. Acta* **105**, 261–274 (2013).
 31. Stoch, J. & Gablankowska-Kukucz, J. The effect of carbonate contaminations on the XPS O 1s band structure in metal oxides. *Surf. Interface Anal.* **17**, 165–167 (1991).
 32. Haber, J., Stoch, J. & Ungier, L. X-ray photoelectron spectra of oxygen in oxides of Co, Ni, Fe and Zn. *J. Electron Spectrosc. Relat. Phenom.* **9**, 459–467 (1976).
 33. Li, Z. *et al.* Fast electrosynthesis of Fe-containing layered double hydroxide arrays toward highly efficient electrocatalytic oxidation reactions. *Chem. Sci.* **6**, 6624–6631 (2015).
 34. Alayoglu, S., Nilekar, A. U., Mavrikakis, M. & Eichhorn, B. Ru-Pt core-shell nanoparticles for preferential oxidation of carbon monoxide in hydrogen. *Nat. Mater.* **7**, 333–338 (2008).
 35. Totir, D., Mo, Y., Kim, S., Antonio, M. R. & Scherson, D. A. *In situ* Co K-edge X-ray absorption fine structure of cobalt hydroxide film electrodes in alkaline solutions. *J. Electrochem. Soc.* **147**, 4594–4597 (2000).
 36. Subbaraman, R. *et al.* Trends in activity for the water electrolyser reactions on 3d M(Ni,Co,Fe,Mn) hydr(oxy)oxide catalysts. *Nat. Mater.* **11**, 550–557 (2012).

37. Leroux, F., Moujahid, E. M., Taviot-Guého, C. & Besse, J.-P. Effect of layer charge modification for Co-Al layered double hydroxides: study by X-ray absorption spectroscopy. *Solid State Sci.* **3**, 81–92 (2001).

Acknowledgements

This work was supported by the National Natural Science Foundation of China (NSFC), the 973 Program (Grant No. 2014CB932102) and the Fundamental Research Funds for the Central Universities (buctylkxj01 and PY201610). We are grateful to Prof. Yury Gogotsi for his insightful and constructive suggestions to this work.

Author contributions

M.S., M.W. and Z.W. proposed the research direction and guided the project. Z.L. and H.D. performed the materials synthesis, characterization and electrochemical tests. J.L. performed the structural characterization. Z.L., H.D., M.S., D.O., M.W. and Z.W. wrote the paper. All authors discussed the results and commented on the manuscript.

Additional information

Supplementary Information accompanies this paper at <http://www.nature.com/>

Competing financial interests: The authors declare no competing financial interests.